Remotely-sensed assessment of the impact of century-old biochar on chicory crop growth using high-resolution UAV-based imagery

Ramin Heidarian Dehkordi, Antoine Denis, Julien Fouché, Victor Burgeon, Jean Thomas Cornelis, Bernard Tychon, Edmundo Placencia Gomez, Jeroen Meersmans

HAL Id: hal-02890286
https://hal.inrae.fr/hal-02890286

Submitted on 6 Jul 2020

Remotely-sensed assessment of the impact of century-old biochar on chicory crop growth using high-resolution UAV-based imagery

Ramin Heidarian Dehkordi[a,b,*], Antoine Denis[a], Julien Fouche[b,c], Victor Burgeon[b], Jean Thomas Cornelis[b], Bernard Tychon[a], Edmundo Placencia Gomez[d], Jeroen Meersmans[b]

[a] Department of Environmental Sciences and Management, University of Liège, Arlon, Belgium
[b] TERRA Teaching and Research Centre, Gembloux Agro-Bio Tech, University of Liège, Gembloux, 5030, Belgium
[c] LISAH, Univ Montpellier, INRAE, IRD, Montpellier SupAgro, Montpellier, France
[d] Urban and Environmental Engineering, University of Liège, Liège, Belgium

ARTICLE INFO

ABSTRACT

In recent years, special attention has been given to the long-term effects of biochar on the performance of agro-ecosystems owing to its potential for improving soil fertility, harvested crop yields, and aboveground biomass production. The present experiment was set up to identify the effects on soil-plant systems of biochar produced more than 150 years ago in charcoal mound kiln sites in Wallonia (Belgium). Although the impacts of biochar on soil-plant systems are being increasingly discussed, a detailed monitoring of the crop dynamics throughout the growing season has not yet been well addressed. At present there is considerable interest in applying remote sensing for crop growth monitoring in order to improve sustainable agricultural practices. However, studies using high-resolution remote sensing data to focus on century-old biochar effects are not yet available. For the first time, the impacts of century-old biochar on crop growth were investigated at canopy level using high-resolution airborne remote sensing data over a cultivated field. High-resolution RGB, multispectral and thermal sensors mounted on unmanned aerial vehicles (UAVs) were used to generate high frequency remote sensing information on the crop dynamics. UAVs were flown over 11 century-old charcoal-enriched soil patches and the adjacent reference soils of a chicory field. We retrieved crucial crop parameters such as canopy cover, vegetation indices and crop water stress from the UAV imageries. In addition, our study also provides in-situ measurements of soil properties and crop traits. Both UAV-based RGB imagery and in-situ measurements demonstrated that the presence of century-old biochar significantly improved chicory canopy cover, with greater leaf lengths in biochar patches. Weighted difference vegetation index imagery showed a negative influence of biochar presence on plant greenness at the end of the growing season. Chicory crop stress was significantly increased by biochar presence, whereas the harvested crop yield was not affected. The main significant variations observed between reference and century-old biochar patches using in situ measurements of crop traits concerned leaf length. Hence, the output from the present study will be of great interest to help developing climate-smart agriculture practices allowing for adaptation and mitigation to climate.

1. Introduction

In the context of mitigating climate change and adapting to the loss of soil fertility, the application of biochar has been promoted during the last decades as a strategy for sustainably improving the soil hydric status and organic matter contents (e.g. Sohi et al., 2010; Malghani et al., 2013; Stewart et al., 2013; Kerré et al., 2017). Biochar is a solid carbon-rich residue of the pyrolysis of biomass produced in an oxygen-limited environment and amended to soil (e.g. Yamato et al., 2006; Montanarella and Lugato, 2013; Lehmann and Joseph, 2015; Trupiano

et al., 2017). Biochar can be obtained from a broad range of feedstocks including manure, wood, and crop residues (Trupiano et al., 2017).

Many efforts have been devoted to providing an indication of the fresh biochar effect on soil properties such as soil acidity, nutrient retention, and water holding capacity (Biederman and Stanley Harpole, 2013; Lehmann et al., 2003; Glaser et al., 2002). For example, de la Rosa et al. (2014) showed that there is a strong positive relationship between the amount of biochar application and soil water holding capacity (WHC) by studying four types of biochar originating from different feedstocks. Glaser et al. (2002) reported that the WHC in terra

preta charcoal-enriched soils of the Amazon basin was higher in comparison to its adjacent reference soils. Abel et al. (2013) also illustrated that biochar could improve the WHC of a sandy soil six months after its application. However, Jeffery et al. (2015) recently indicated that biochar had no significant impact on either the sandy soil WHC or plant available water content in a naturally restored grassland located in Ede (The Netherlands). Similarly, Gray et al. (2014) confirmed no significant effects of biochar produced from feedstocks of hazelnut shells and Douglas fir chips on plant available water content in a clay-loam soil in Western Oregon, United States. A recent study by Schneider et al. (2020) reported a higher water content for relict charcoal hearths in the forest area of the Tauersche Forst, Germany for wet conditions versus a lower water content under dry conditions. Major et al. (2010) stated greater nutrient availability, especially in Ca and Mg, in charcoal amended tropical soils of savannas in Colombia; they also demonstrated a higher grain yield for maize for up to at least four years after the application of biochar. The higher nutrient availability (Ca and Mg) was also found in similar charcoal-rich cultivated soils in Wallonia (Hardy et al., 2017a).

A commonly documented impact of biochar is the improvement of aboveground crop biomass productivity. Using a quantitative global-scale approach, Jeffery et al. (2011) found an average increase in crop productivity of 10 % as a result of biochar addition in tropical soils. Similarly, Simon et al. (2017) reported an average crop yield increase of 25 % with biochar application in arable tropical soils, whereas no influence was found in temperate latitudes. Meta-regression analyses showed that crop yield response increases over time after the initial addition of biochar, i.e. an increase of 7 % and 12 % in the second and fourth year post biochar application, respectively (Crane-Droesch et al., 2013). Biederman and Stanley Harpole (2013) reported a significant positive short-term impact of biochar on aboveground crop productivity and yield through a comprehensive meta-analysis of 371 independent experiments. Likewise, large short-term yield increases of cow pea were found in Manaus, Brazil, after charcoal amendments to highly weathered tropical soils (Lehmann et al., 2003). However, both short-term agronomical benefits of biochar (few years after the application) and long-term effects (up to few centuries after application) should be studied. Although, there is a general lack of studies focusing on long-term effect, Hernandez-Soriano et al. (2016) illustrated a long-term impact of biochar with an average increase of 10 % in the aboveground dry biomass of maize by studying 12 different kiln sites within 5 different arable fields in Wallonia, Belgium, during autumn 2014. In contrast, evidence of plant growth diminution as a consequence of biochar application has been found in some instances. Mikan and Abrams (1986) indicated significant growth depression of both white and red oak over the historic charcoal hearth sites of Pennsylvania, United States. Mastrolonardo et al. (2019) also observed that average values of tree ring width (European beech and silver birch) decreased even though soil nutrient status was improved in a silty soil (Belgium). It was argued that biochar addition could inhibit the promotion of plant growth as observed with wheat and radish biomass decrease in loamy calcarosol amended with fertiliser taken from Victoria, Australia (van Zwieten et al., 2010). Another study by Güereña et al. (2013) has corroborated this reductive impact of biochar incorporation by reporting no improvement of maize crop growth in fertile temperate soils over a long-term study from 2007 to 2010.

Despite the growing body of literature on biochar incorporation into the soil, accurate monitoring of the observed long-term agronomic effects on crop growth remains largely elusive. Yet, understanding long-term effects in agro-ecosystems is important as long-term biochar accumulation in soils significantly impact soil physico-chemical and microbial properties in agricultural fields affected by relic charcoal hearths (Hardy et al., 2017a, b; Hardy et al., 2019). Remote sensing is proposed as an approach to provide detailed information regarding spatial and temporal variations in crop status for precision agricultural monitoring (Gevaert, 2015). In recent decades, numerous satellite

products have been used to support agricultural applications (Mulla, 2013). Although high spatial, spectral, and temporal resolution data needed for precision agriculture applications can currently be obtained from satellite imagery (e.g. Sentinel-1 SAR), optical remotely-sensed data acquisition (e.g. Sentinel-2) is often difficult during growing seasons as these periods are often characterized by cloud cover (Gevaert, 2015; Clevers et al., 2017). Moreover, a detailed monitoring of crop dynamics is particularly critical when considering high-value crops to improve decision-making associated with precision crop management at the subfield scale (Zipper and Loheide, 2014). High-resolution airborne remote sensing data either from low-altitude manned aircrafts or unmanned aerial vehicles (UAVs), has recently been proposed as a way to fill this gap (Xia et al., 2016). It is important to note that the main restriction of UAV-based remote sensing is that its image acquisition is paired with operational costs and efforts, which may therefore reduce the temporal frequency of the UAV imagery as well as limit the size of the monitoring area (Gevaert, 2015).

High-resolution RGB, multispectral and thermal UAV imageries have been widely promoted in recent years because of their ability to provide plant physiology, vegetation characteristics, and crop water status at the canopy scale improving the site-specific decision-making process in a precision agriculture context (Gago et al., 2015; Berni et al., 2009b). Regarding biochar impacts on plant systems, there are no studies available using high-resolution UAV-based data at canopy level over a cultivated field enriched with century-old biochar patches. In this study, we will focus on investigating the impacts of century-old biochar enrichment on crop growth at canopy level for the first time using UAV imagery.

Airborne RGB and multispectral imageries are capable of providing crucial crop structural parameters like canopy cover and leaf area index (LAI), together with the narrow-band multispectral vegetation indices that provides relevant information about photosynthesis and plant functioning (Gago et al., 2015; Berni et al., 2009b). A new era of UAV-based thermal remote sensing is emerging with the high-resolution modelling of spatially distributed crop water status parameters such as stress or evapotranspiration (Berni et al., 2009a). Deficiency in the plant available water content is defined as the crop water stress (Ihuoma and Madramootoo, 2017), and leads to leaf stomatal closure, reduction of the transpiration rate and the evaporative cooling, and will consequently increase the leaf temperature (Berni et al., 2009a; Zarco-Tejada et al., 2013). Mapping the crop water stress over discontinuous canopies is seen as the benchmark capability of UAV-based thermal remote sensing (Berni et al., 2009a, b). High-resolution UAV-based thermal imagery is able to detect the incidence of water stress by monitoring the canopy temperature with thermal infrared sensors (Berni et al., 2009a; Zarco-Tejada et al., 2013; Gago et al., 2015). Thus, thermal remote sensing is capable of early detection of water scarcity related to drought over agricultural fields, which are essential features for managing irrigation schedules and various environmental activities (Tanriverdi et al., 2017). Crop water stress is a function of air and canopy temperatures together with the vapour pressure deficit (Bellvert et al., 2014; Gago et al., 2015). The difference between canopy surface temperature (T_c) and air temperature (T_a), is a widely accepted indicator of crop water stress (Jackson et al., 1977; Bellvert et al., 2014; García-tejero et al., 2016) which can be derived from UAV-based thermal images.

A last important point to address is that crop water stress might be highly affected by topography because soil water content, and hence, the canopy temperature depend on topography, which is a dominant factor influencing hydrological processes such as groundwater flow (Seibert et al., 2006). Therefore, a more specific evaluation of the canopy temperature as a function of biochar presence is of great interest in order to mitigate information redundancy due to the field topography. Over the past few years, the usage of digital elevation model (DEM)-based topographic indices has gained increasing attention for predicting the spatial distribution of soil moisture, which imposes a

significant ecohydrological impact on the vegetation composition in accordance with the site tendency to receive or evacuate water from up-land and down-land areas, respectively (Kopecký and Čížková, 2010). The topographic wetness index (TWI) is a well-known terrain derivative that reveals the potential spatial variation of soil wetness and surface saturation conditions (Grabs et al., 2009).

This manuscript describes the impacts of century-old biochar using high-resolution UAV remote sensing data in combination with *in situ* measurements of soil properties and crop traits. We examined the effects of century-old charcoal-enriched kiln sites, produced from beech and oak forests in Wallonia more than 150 years ago on chicory crop growth. The advanced perspectives of UAV remote sensing for monitoring the temporal dynamics of crops affected by century-old biochar enrichment in precision agriculture are addressed.

2. Materials and methods

2.1. Study area

The study area was an agricultural field with chicory (*Cichorium intybus* subsp. *intybus* convar. *Sativum*) of approximately 13 ha located near Isnes (NW corner: 50°31′N 4°44′E; SE corner: 50°31′N 4°45′E), central Belgium. The climate of the area is temperate with dry and hot summers and 30-year (1987–2017) average annual temperature and precipitation of 9.6 °C and 889.42 mm, respectively. This field is comprised of 13 century-old biochar-enriched patches resulting from historical charcoal production in mound kiln sites of oak, hornbeam, beech, and hazel forests dating to more than 150 years ago (for a more detailed description, the reader is referred to Hardy et al., 2017b). The century-old biochar-enriched patches are apparent as darker black spots of nearly 25 m diameter (Fig. 1). Apart from these biochar-enriched

Fig. 1. The experimental area within the chicory field revealing the composition of the 11 pairs of biochar-enriched versus reference plots as well as the location of the ground control points. Century-old biochar-enriched patches are visible as darker black ovals. An RGB orthomosaic image captured by the unmanned aerial vehicle on the 22th May of 2018 is used as the background.

patches, the experimental field has homogeneous soil conditions: Luvisol with a silt loam texture in the topsoil. The agricultural practices are homogenous throughout the field. Eleven 10 m × 10 m plots (red squares in Fig. 1) were designed inside the biochar-enriched patches, at least 3 m from the border of each patch in order to avoid gradient effects at the edge of the biochar-enriched patches. The two remaining patches were instrumented for another experiment and hence were not used in the present study. Subsequently, eleven plots of 10 by 10 m (blue squares in Fig. 1) were created over adjacent reference soil areas within a distance of approximately 45 m from the biochar-enriched patches in order to prevent the plausible mixing of biochar and reference soil particles due to ploughing activities. It is worth mentioning that each biochar-enriched patch was located on the same management strip (NW-SE direction) as the corresponding reference patch to avoid variation in treatment effects between the strips. Five black and white tiles of 65 cm × 65 cm, were deployed throughout the study field (Fig. 1) as ground control points (GCPs) to optimise the geo-referencing and alignment of the acquired UAV images which enables a precise time-series analysis at the pixel-to-pixel level. The centroid coordinates of the GCP targets were determined using a real-time kinematic GPS (RTK-GPS) with ~3 cm horizontal accuracy.

2.2. Statistical analysis

Statistical global and paired *t*-tests were conducted to examine the influence of century-old charcoal kiln sites on the crop growth. A *t*-test indicates the statistical significance of the difference between two groups of data assuming the normal distribution of each data set (Kim, 2015). Paired t-tests consider the independence of the pairs which is an important constraint in this study. First, the normality of the observed differences was confirmed using the Shapiro-Wilk normality test (Shapiro and Wilk, 1965). Then, the paired and global t-tests were applied to identify the significance of the observed differences between the pairs of biochar-enriched and reference plots.

It is worth noting that the small number of available observations, i.e. 11 paired sites (reference versus biochar-enriched), did not guarantee using goodness of fit measures such as coefficient of determination (R^2) in this study. Therefore, we checked the significance of the attained R^2 value between the UAV-based imageries and soil properties or crop traits using the statistical F-test. We also applied the non-parametric Kendall's rank correlation tau (τ) test which is less sensitive to the small statistical sample size (Kendall, 1938) to further assess the significance of the obtained correlations.

2.3. In situ and laboratory measurements

2.3.1. Soil organic carbon and nitrogen contents

A regular sampling method, comprised of 5 soil subsamples was followed in each of the 22 experimental plots, totalling 110 subsamples over the entire field on the 11th of October 2018. The subsamples were spatially distributed within each plot in order to better capture the potential intra-plot variability. Initially, five random subsamples per plot were obtained using a hand-held soil auger applied to a reference depth of 10 cm. It should be highlighted that prior to the soil sampling, the soil was ploughed to a depth of nearly 30 cm. Next, the five subsamples of each plot were evenly blended together resulting in one composite sample per plot (22 samples for the entire field). Then, the soil samples were passed through a 2 mm sieve to separate soil fine earth with a minimum quantity of 200 g per sample in order to facilitate the laboratory soil analysis. Prior to the laboratory analysis the samples were oven-dried at 40 °C until they reached a constant weight. The soil samples were analysed for the quantification of organic carbon (ISO 10694:1995, 1995), and total nitrogen (ISO 13878:1998, 1998) concentrations. Organic carbon and total nitrogen were analysed by dry combustion using the Leco TruMac element analyser.

2.3.2. Crop traits

One intention of this study was to observe the variations in bio-physical plant growth indicators, for instance the differences in plant yield, induced by biochar presence in the soil. Non-invasive measurements of crop traits were performed on the 15th of June 2018. This dataset assessed the impact of biochar on the leaf length (using a measuring tape) and chlorophyll content (using a hand-held Opti-Sciences CCM-200 chlorophyll content meter) of the chicory crop. The CCM-200 reading represents the chlorophyll content index (CCI) based on the leaf transmittance values of the spectral bands centred at 653 and 931 nm. A regular sampling method of 25 measurements in each of the 22 experimental plots, totalling 550 measurements of leaf length and chlorophyll content were carried out. In this case, each measurement was made on the most developed leaf of the plant selected for data acquisition, and the leaves were also visually checked to avoid any potential disease. For each plot, the 25 measurements were spatially distributed over the plot to better represent intra-plot variability. The median of 25 measurements made within each plot (i.e. median used instead of mean in order to avoid the possible bias introduced by outliers) were used to describe the canopy in each experimental plot.

A set of destructive crop trait measurements were performed on plant roots and leaves. This sampling took place on the 6th and 7th of September 2018, a few days before the harvest date. Destructive field measurements are usually time-consuming and expensive. As a result, in the destructive sampling campaign three randomly selected rows of 0.5 m length consisting of approximately 10 chicory plants were collected in each of the 22 test plots, totalling 66 samples (for nearly 660 plants) for the entire field. The median of the 10 plants in each plots was used. Fresh weight and yield of leaves were measured in the field immediately after sampling, leaf dry weight was measured in the laboratory after oven-drying the leaves at 80 °C until a constant weight was reached in order to compute leaf dry matter content. Similarly, root yield, length, and perimeter at the soil surface level were measured to obtain data as regards root characteristics. A previous study by Abawi (1998) reported that specific soil conditions, such as excess soil moisture or high contents of organic acids (i.e. C/N greater than 30), could induce forking in carrot plants. Therefore, we also measured the number of forks and number of cracks in the collected chicory roots. The hypothesis was that charcoal presence in the soil would reduce the compactness of its particles, thereby becoming highly desirable for root growth and avoiding the possible physiological disorders such as cracking and forking.

2.4. UAV-based imageries

2.4.1. Airborne campaigns and image processing

A total of 13 flights were executed over the 2018 growing season (Table 1) using RGB, multispectral and thermal cameras on board of two UAVs. A DJI Phantom 4 Pro (DJI, Nanshan, Shenzhen, China) was

Table 1

An overview of the unmanned aerial vehicle flights over the year 2018. Flight times are provided in local time.

Date		UAV imagery		
Month	Day	RGB	Multispectral	Thermal
April	19	11h	—	—
May	09	11h	—	—
	22	10h	—	—
June	05	12h	—	—
	15	11h	—	—
	22	11h	—	—
July	05	10h	12h	12h
	13	10h	13h	13h
	24	10h	12h	—
August	07	—	12h	12h

flown over the chicories at 65 m altitude above ground level (AGL) at nadir, field of view (FOV) of 84°, an airspeed of 5 ms^{-1}, with 85 % front and 75 % side image overlaps obtaining 5472 × 3648 pixel RGB images. With these specifications, the resulting ground sampling distance (GSD) was 1.8 cm. We planned DJI Phantom 4 Pro UAV flights using Pix4D capture software (Pix4D S.A., Lausanne, Switzerland).

The second set of UAV images were acquired from a DJI Matrice 100 (DJI, Nanshan, Shenzhen, China), a quadcopter with a flight endurance of 30 min using two TB48D 5700 mA h batteries simultaneously, which was developed to carry the multispectral and thermal sensors concurrently. The multispectral sensor used was a MicaSense RedEdge-M integrated with MicaSense downwelling light sensor (MicaSense, Seattle, WA, USA) with five discrete narrow bands comprising blue (475 nm centre wavelength, 20 nm bandwidth), green (560 nm, 20 nm), red (668 nm, 10 nm), red-edge (717 nm, 10 nm), and near-infrared (840 nm, 40 nm). The FLIR Vue Pro Radiometric thermal imager (640 × 412 pixels, 13 mm lens, and 9 Hz frequency) with spectral response in the range of 7.5–13 µm was used together with the FLIR GPS geo-tagger (FLIR, Oregon, USA) to conduct the thermal imagery. The UAV flight path of DJI Matrice 100 was planned using Atlas Flight software (MicaSense, Seattle, WA, USA). The flight altitude was set at 60 m AGL, an airspeed of 7 ms^{-1}, and with 75 % forward and sideways image overlap resulting in a spatial resolution of 3.7 cm and 7 cm for multispectral and thermal images, respectively. Neither multispectral nor thermal data were acquired before July 2018 (Table 1) since the Matrice 100 platform was developed at the end of June 2018.

Acquired RGB images were processed using Pix4Dmapper photo-grammetric software (Pix4D S.A., Lausanne, Switzerland). The processing chain includes: (i) aerial triangulation and geometric correction using the ground control point coordinates obtained from the DGPS to assign the high accuracy geo-coordinate system to the photogrammetric block, (ii) construction of the dense point cloud and mesh, (iii) ortho-rectification of the images, and (iv) derivation of the digital surface model (DSM) along with the RGB orthomosaic (Fig. 2).

Likewise, the multispectral imagery was processed using Pix4Dmapper software following the same photogrammetric processing chain. MicaSense calibrated reflectance panels with known reflectance values (MicaSense, Seattle, WA, USA) were captured immediately before and after each flight. Therefore, the radiometric calibration chain used the calibration coefficients of the reflectance panels along with the ISO values recorded by the downwelling light sensor (DLS) to convert the raw image digital number (DN) to the calibrated reflectance values (Fig. 2).

Thermal images were initially geo-tagged during the UAV flights using the integrated FLIR GPS geo-tagger. The brightness temperature values were translated to the land surface temperature (LST) through the FLIR UAS application (FLIR, Oregon, USA) and Pix4Dmapper by applying the local recorded air temperature, humidity, and emissivity values. The same photogrammetric alignment and geometric correction was applied using the coordinates of the GCPs to generate the high-resolution temperature index maps over the study site (Fig. 2).

2.4.2. RGB canopy cover

The ratio of the pixels covered by vegetation to the total number of ground pixels, named the canopy cover, is a widely used biophysical indicator of the crop growth stage in remote sensing-based environmental applications (Trout et al., 2008; Johnson et al., 2012). In the present study, the canopy cover was derived from the high-resolution UAV-based RGB orthomosaic image, with the GSD of 1.8 cm, which enables the accurate classification of the study area into vegetation and non-vegetation pixels. For all the pixels within the orthomosaic image we calculated the difference between the spectral response of the green band and the corresponding values of the blue and red channels as follows:

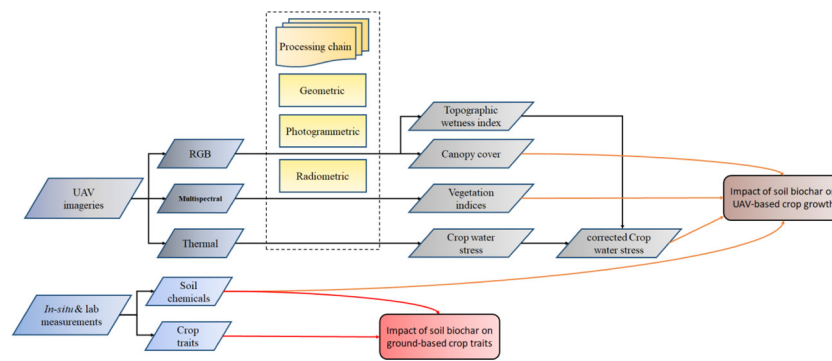$$[(DN_{green} - DN_{blue}) = \alpha] \text{ and } [(DN_{green} - DN_{red}) = \beta] \tag{1}$$

Fig. 2. Methodological flowchart to assess the impact of biochar on soil-plant systems.

where DN$_{blue}$, DN$_{green}$, and DN$_{red}$ represent the digital numbers (DNs) of the blue, green and red parts of the visible spectrum, respectively.

This classification equation was established using the fact that the spectral signature of vegetation reveals a slight peak in the green band of the electromagnetic spectrum compared to the blue and red spectral channels (Parece and Campbell, 2015). Pixels with both α and β greater than 20 were classified as vegetation since this threshold yielded the best vegetation clustering results from the visual inspection (Fig. 2).

2.4.3. Multispectral vegetation indices

Several narrow-band vegetation indices were calculated from the multispectral imagery to examine whether the impact of biochar on the crop performance could be captured by the high-resolution UAV-based multispectral remote sensing. Table 2 summarises the vegetation indices evaluated in this research. The normalised difference vegetation index (NDVI) (Rouse Jr et al., 1974) was determined to indicate the vegetation coverage within the study plots following:

$$NDVI = (R_{NIR} - R_{red}) / (R_{NIR} + R_{red}) \qquad (2)$$

where R$_{red}$ and R$_{NIR}$ are the processed reflectance values of the red and near-infrared spectral bands of the MicaSense RedEdge-M sensor, respectively.

It is generally assumed that the normalised difference vegetation index (NDVI) provides a robust indication of photosynthetic activity as well as vegetation greenness (Rouse et al., 1974; Schmidt and Karnieli, 2001), since vegetation has the highest rates of absorption and reflection in the red and NIR bands, respectively. However, there are further merits of using NDVI to retrieve pure vegetation and soil pixels due to the fact that the index is highly sensitive to soil brightness and background effects, as was raised by Huete (1988) and Schmidt and Karnieli (2001). To address such background effects, the weighted difference vegetation index (WDVI) developed by Clevers (1989) was further computed based on Eq. (3). WDVI explicitly considers that the ratio between NIR and red reflectance values over the bare soil is constant and also independent of soil moisture content (Clevers, 1989).

$$WDVI = R_{NIR} - a.R_{red} \qquad (3)$$

where a is the slope of soil line which can be derived as the ratio of the NIR to red band reflectance values over the bare soil; Rred and RNIR are the reflectance values in the red and near-infrared portions of spectrum, respectively.

Clevers (1989) concluded that the WDVI is an appropriate index for most soil types. Moreover, WDVI is less sensitive to the saturation of the chicory leaves, as opposed to NDVI, when the crop is at the end of its growth stage. As a result, UAV-based WDVI could lead to a better separation of soil and vegetation pixels than NDVI imagery. Therefore, WDVI was used instead of NDVI to create a multispectral based vegetation mask. It is worth mentioning that we were interested in evaluating the plant healthiness as well as vegetation greenness as a function of biochar presence and hence only the vegetation pixels were

monitored in the multispectral analysis. First, a threshold of WDVI higher than 0.45 was applied to the WDVI imagery with 3.7 cm GSD to extract the so-called true canopy pixels in which the pixels are entirely covered by vegetation. This threshold provided the best vegetation mask according to the visual inspection. Second, the obtained WDVI-based vegetation mask was used to remove the soil pixels from the determined vegetation indices. Apart from the two above-mentioned structural indices, three chlorophyll indices (Table 2) were also computed to perform a detailed analysis of the information provided by UAV-based multispectral imagery. Similar to the structural indices, the created WDVI-based mask layer was used to remove the soil pixels from the multispectral analysis of the retrieved chlorophyll indices.

2.4.4. Crop water stress and Topographic wetness index modelling

Meteorological data was retrieved from a local automated weather station situated in the middle of the study field. Meteorological data was recorded as 30 min averages, including air temperature, precipitation, wind speed and direction, relative humidity, and solar radiation. First, the computed RGB-based vegetation mask (Section 2.4.2) was resampled to the spatial resolution of the thermal images using the nearest neighbour algorithm in order to retrieve the true canopy pixels from the thermal imagery. Then, the air temperature recorded by the local weather station at the UAV overpass time (Table 1) was used to determine the implemented T$_c$ – T$_a$ index as the crop water stress indicator. It is important to highlight that the developed Matrice 100 platform at 60 m flight altitude enabled the thermal image acquisition to cover the entire field in approximately 30 min, and hence, a constant value of air temperature was used to model T$_c$ – T$_a$ for each recording date. All the thermal flights were executed around noon (Table 1) which is the optimum time to obtain thermal imageries in order to avoid the shaded leaves and variability of stomatal closure in leaf water status (Bellvert et al., 2014). Moreover, the sky condition was clear with no clouds over the study field during the thermal acquisitions. To assess the case where a complete impact of biochar on the crop water stress over the entire growing season is available, we computed the mean T$_c$ – T$_a$ value of the three monitoring dates (Table 1).

Traditional topographic wetness index (T-TWI) and system for automated geoscientific analyses wetness index (SAGA WI) are the most widely applied algorithms in advanced geographic information systems (GIS) software packages such as Quantum GIS (QGIS) for modelling the topographic wetness index based on remote sensing inputs (Kopecký and Čížková, 2010; Aksoy et al., 2016). TWI was computed as (Aksoy et al., 2016):

$$TWI = \ln [\alpha / \tan(\beta)] \qquad (4)$$

where α is the local contributing drainage area that reflects the tendency of water flow from upslope and β is the angle of the local topographic slope in radians.

Aksoy et al. (2016) illustrated that SAGA WI generates more realistic estimates of the topographic wetness index than T-TWI with

Table 2
Vegetation indices investigated in the present study.

Abbreviation	Index name	Formulation	Indication	Reference
NDVI	normalized difference vegetation index	$(R_{NIR} - R_{red}) / (R_{NIR} + R_{red})$	Structural index, photosynthetic activity and vegetation greenness	(Rouse Jr et al., 1974)
WDVI	weighted difference vegetation index	$WDVI = R_{NIR} - a.R_{red}$ with $a = (R_{NIR} / R_{red})$ of the soil	Crop physiological traits	(Clevers, 1989)
NDRE	normalized difference red edge index	$(R_{NIR} - R_{rededge}) / (R_{NIR} + R_{rededge})$	Crop nitrogen concentration	(Siegmann et al., 2012)
CI-red	chlorophyll index red	$(R_{NIR} / R_{red}) - 1$	Canopy chlorophyll and biomass	(Similar to Clevers et al., 2017)
s-CCCI	simplified canopy chlorophyll content index	NDRE / NDVI	Canopy chlorophyll	(Similar to Fitzgerald et al., 2006)

respect to SAGA modified catchment surface determinations. Therefore, SAGA WI was used in the present study to model the topographic wetness index over the study field. For this, the RGB flight on the 9th of May 2018 (Table 1) was executed over the entirely bare soil ground following a so-called double grid pattern consisting of perpendicular flight lines with 85 % frontal and 75 % side overlap in order to capture the highest terrain discrepancies in terms of topography elements. The obtained DSM from the UAV imagery over the bare soil field is equal to a digital terrain model (DTM) that only reflects the terrain surface topography.

It is worth drawing attention to the fact that both current versions of T-TWI and SAGA WI are dedicated to moderate and high spatial resolution satellite remote sensing inputs ranging from 30 to 0.5 m. As a result, very high-resolution UAV-based DTM image (spatial resolution of 1.8 cm in the current study) would lead to noisy TWI patterns in the outcome of the SAGA WI modelling approach. In other words, the higher resolution the inputs are, the noisier the outcome is. Thus, the acquired DTM from the UAV imagery was initially pre-processed to smooth abnormal alterations in the elevation map caused by noisy micro-topographic details. Pre-processing of the UAV-based DTM was carried out using a rectangular 3×3 low-pass focal-modal digital filter (corresponding to 5.4×5.4 m) with a relatively higher power on the rows than the columns due to the fact that the major tractor driving paths, as the main source of the micro-topography changes in elevation, were apparent vertically within the study field. Next, the primary topographic attributes (i.e. slope, aspect, and curvature) were derived from the post-processed DTM and were fused in SAGA WI to model secondary topographic derivatives such as the topographic wetness index over the test area.

We used a multivariable function based on the UAV-based thermal and TWI imageries to mitigate the impact of topography on the canopy temperature as follows:

$$T_c \text{ (TWI corrected) (i)} = T_c \text{ (i)} - [f \text{ (TWI) (i)} - T_c \text{ (TWI median) (i)}]$$

(5)

where T_c (TWI corrected) is the retrieved pure canopy temperature while mitigating the topography impact, T_c is the pure canopy temperature after removing the soil background pixels, f (TWI) is the regression function of T_c based on TWI imagery considering all the reference and biochar-enriched plots, T_c (TWI median) is the predicted canopy temperature for a given value of TWI which is the median value of TWI imagery combining all the experimental pairs, and index i represents the experimental plots.

It is worth noting that the aforementioned thermal amendment was applied separately for each acquisition date. As such, the identified linear regression fits between TWI and T_c - T_a for each acquisition date were used to mitigate the impact of topography on the crop water stress and the corrected T_c - T_a values were calculated. Finally, we computed the mean corrected T_c - T_a values of the three thermal acquisitions (Fig. 2).

3. Results and discussion

3.1. Soil organic carbon and nitrogen contents

The biochar-enriched sites were found to be characterized by significantly higher soil organic carbon (SOC) and nitrogen contents (Fig. 3a), which was also reported by Biederman and Stanley Harpole (2013) and de la Rosa et al. (2014). More specifically, the largest effect was observed in the total nitrogen content (i.e. *t*-test p-value = 0.00006) with a median total nitrogen content for the biochar-enriched soils of 0.15 % (expressed as grams of N per 100 g of dry soil (gN/100 g)) compared to 0.12 % for the reference soils. Moreover, (SOC) content is 1.9 % (gC/100 g) for the biochar-enriched soils, whereas this is only 1.3 % for the reference soils (which is significantly
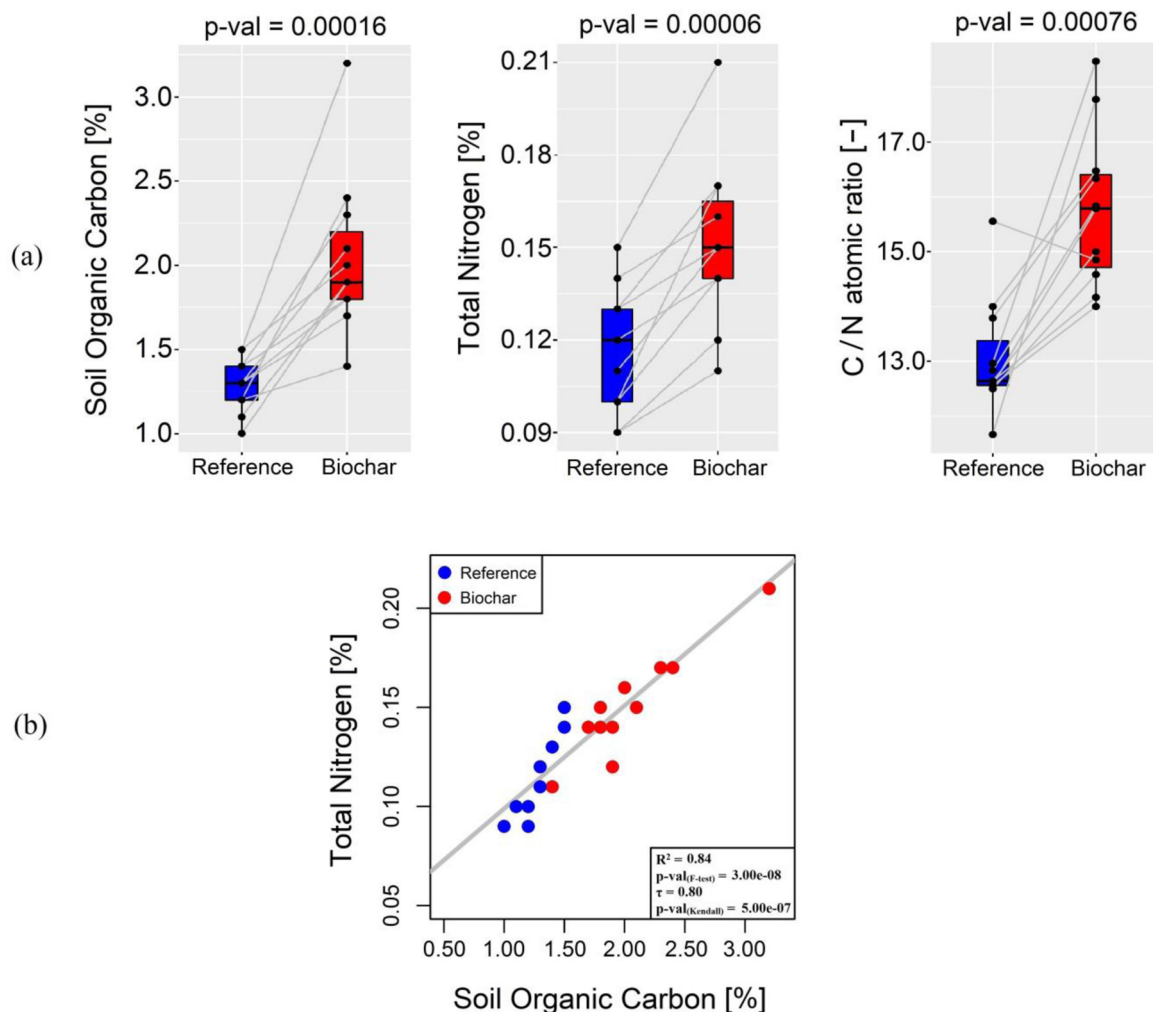
Fig. 3. (a) Comparison of soil organic carbon (SOC), total nitrogen, and C/N atomic ratio between the reference and biochar-enriched plots following the statistical paired *t*-test. The horizontal black line represents the median value, surrounded by box edges presenting the 25th and 75th percentiles. The black circles represent the experimental plots of each pair and the grey line between the points compares the corresponding reference and biochar-enriched plots of each pair. (b) Relationship between soil total nitrogen (y-axis) and soil organic carbon (x-axis) for all the 11 experimental pairs, the blue and red circles represent the reference and biochar-enriched plots, respectively and the grey line indicates the linear regression fit. (For interpretation of the references to colour in this figure legend, the reader is referred to the web version of this article).

different with a p-value = 0.0001). Also the atomic SOC to total nitrogen ratio (C/N) was significantly higher (p-value = 0.0007) in the biochar-enriched soils (15.7) as compared to the reference soils (12.6). Consequently, SOC was strongly correlated with total nitrogen when considering all the reference and biochar-enriched plots (R^2 = 0.84, p-value$_{(F-test)}$ = 3.00e-08) as shown in Fig. 3c (Kendall's τ coefficient = 0.80, p-value$_{(Kendall)}$ = 5.00e-07).

3.2. Crop traits

The results of the non-destructive crop trait measurements taken on the 15th of June 2018, are presented in Fig. 4a. Chicory leaf length was significantly different with 26 ± 1.72 cm in the reference plots and 30 ± 1.58 cm for the biochar-enriched plots (p-value = 0.00040). All the biochar-enriched plots reported longer chicory leaves than the corresponding reference plots, except for plot 2 where the leaf length was equal (28 cm) for both biochar-enriched and reference plots. In contrast, the chlorophyll content was not significantly different (p-value = 0.619) between treatments (Fig. 4a).

Fig. 4b-c shows a comprehensive overview of the destructive *in situ* measurements. In light of the weak statistical differences (p-value > 0.1) obtained for all the examined plant biophysical parameters, no

significant influence of biochar can be illustrated. The biochar chicory leaves exhibited a median yield value of 26.62 ± 5.56 t.ha^{-1}, versus 26.40 ± 4.31 t.ha^{-1} for the reference leaves, resulting in a paired *t*-test p-value of 0.1. The leaf dry matter content revealed no statistical difference between treatments (p-value = 0.24). This slight promotion of the aboveground productivity as a consequence of biochar presence is in line with several previous studies (Major et al., 2010; Hernandez-Soriano et al., 2016; Kerré et al., 2017).

Chicory root perimeter, length, and yield were not significantly different between the reference and biochar-enriched plots (p-value = 0.36, p-value = 0.41, and p-value of 0.34 respectively). These results differ from the total root mass increase of maize observed by Yamato et al. (2006). Discrepancies in the physiological disorder of chicory roots, either potential forking or cracking caused by biochar presence, were not observed (Fig. 4c).

3.3. UAV-based indices

3.3.1. RGB canopy cover

First, the canopy cover of the eleven experimental pairs (Fig. 1) was evaluated. Fig. 5a shows the temporal profiles of the canopy cover percentage for the biochar-enriched plots in comparison to the
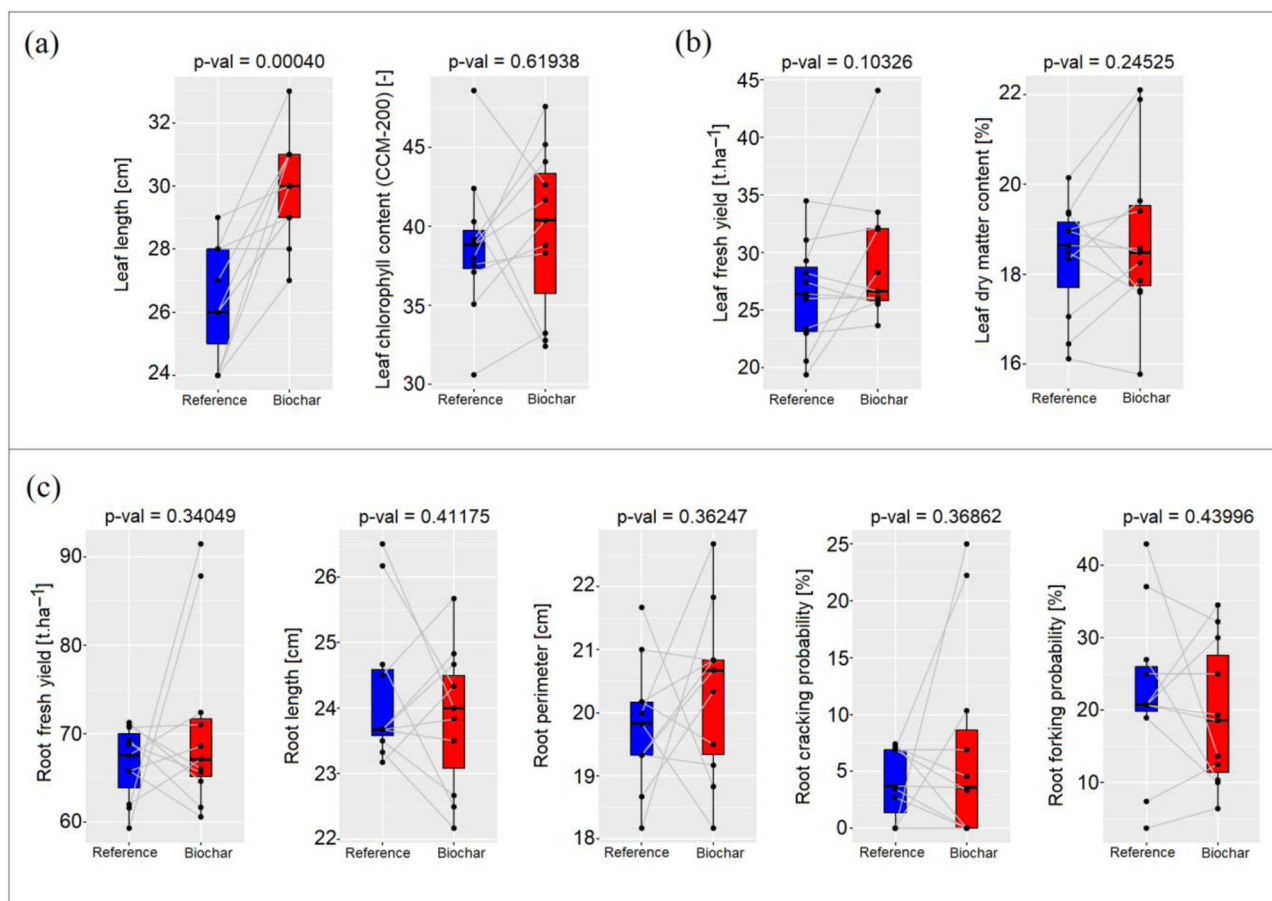
Fig. 4. Impact of biochar presence on the biophysical plant growth parameters for non-destructive leaf structural traits on the 15th of June 2018 (a), destructive measurements of leaves (b) and roots (c) on the 6th and 7th of September 2018. The statistical significance of the difference for each parameter is expressed as the p-value of the paired *t*-test. The horizontal black line represents the median value, surrounded by box edges presenting the 25th and 75th percentiles. The black circles represent the experimental plots of each pair and the grey line between the points compares the corresponding reference and biochar-enriched plots of each pair.

reference plots. The canopy cover displayed greater values in biochar-enriched plots over the green-up phase, except for plots 8 and 10. The area under the curve (AUC) of the canopy cover yielded a significant statistical difference (p-value = 0.00032) between the biochar-enriched and reference plots (Fig. 5b). In addition, the global T-test of the AUC-canopy cover confirmed a significant positive impact of biochar presence on the crop growth (p-value = 0.00038) counting the entire dataset regardless of the other potential effects. This finding is in accordance with the positive growth of maize observed by Kerré et al. (2017) who also studied relict charcoal hearths in Belgium.

As stated before, the destructive *in situ* dataset was collected on the 6th and 7th of September 2018 at the end of the growing season and a few days prior to the harvesting period. The analysis of the UAV-based canopy cover indicated that it is worthwhile to pay more attention to the plant biophysical indicators during the green-up phase in order to have a better assessment of the impact of biochar on the crop growth. However, a more detailed evaluation is needed to completely evaluate the biochar amendment feedback in this regard. We recommend developing further sampling schemes that account for the temporal effects associated with phenology. High frequency sampling schemes would also help to provide a better interpretation of the results.

Delta area under the curve (AUC) of canopy cover exhibited no linear relationship with delta SOC (Fig. 6a). Similar to the delta SOC results, the UAV-based canopy cover showed no relationship with delta total nitrogen, nor with C/N atomic ratio (Fig. 6b-c).

To assess the cause of these weak relationships, the key assumptions related to the design of the experimental plots were examined. Looking at the scatterplots (Fig. 6a–c), one plot (plot 3) displayed the highest

value of delta AUC of canopy cover with a low delta SOC that did not align with the other pairs. We split the data into delta AUC of canopy cover and delta SOC. Plot 3 was detected as an outlier based on the median absolute deviation test of delta AUC of canopy cover. In addition, one plot (i.e. plot 1) showed the highest value in delta SOC while having a low delta AUC of canopy cover (Fig. 6a–c). Subsequently, plot 1 was detected as an outlier through the median absolute deviation test of delta SOC.

To investigate whether the detected outliers closely matched the real field constraints, we specifically focused on the location of the experimental plots along with the SOC and nitrogen contents of the soil samples. Although plot 1 revealed the highest delta SOC, the impact of charcoal presence on the canopy cover growth was not of particular concern which is likely due to the presence of shadows from the adjacent trees located in the west of the field (Fig. 1) and the associated impacts on the soil moisture. Also, plot 1 measurements may have been affected by litter fall of these trees (Schwendenmann, 2015). It is worth mentioning that high-resolution UAV-based DSM imagery indicated that pairs 1 and 3 are the only experimental pairs which are situated in the part of the study field where the slope is towards the northwest (image not shown) which may reduce the likelihood of facing the sun illumination. In addition, the TWI imagery showed its two first highest values in biochar-enriched plot 1 (TWI = 9.02) and biochar-enriched plot 3 (TWI = 6.79) indicating high soil moisture potentials in the detected outliers.

After removing these two outliers, delta SOC yielded a linear relationship (Fig. 6d) with delta AUC of canopy cover (R^2 of 0.48 and p-value$_{(F-test)}$ = 0.038). The obtained correlation was statistically
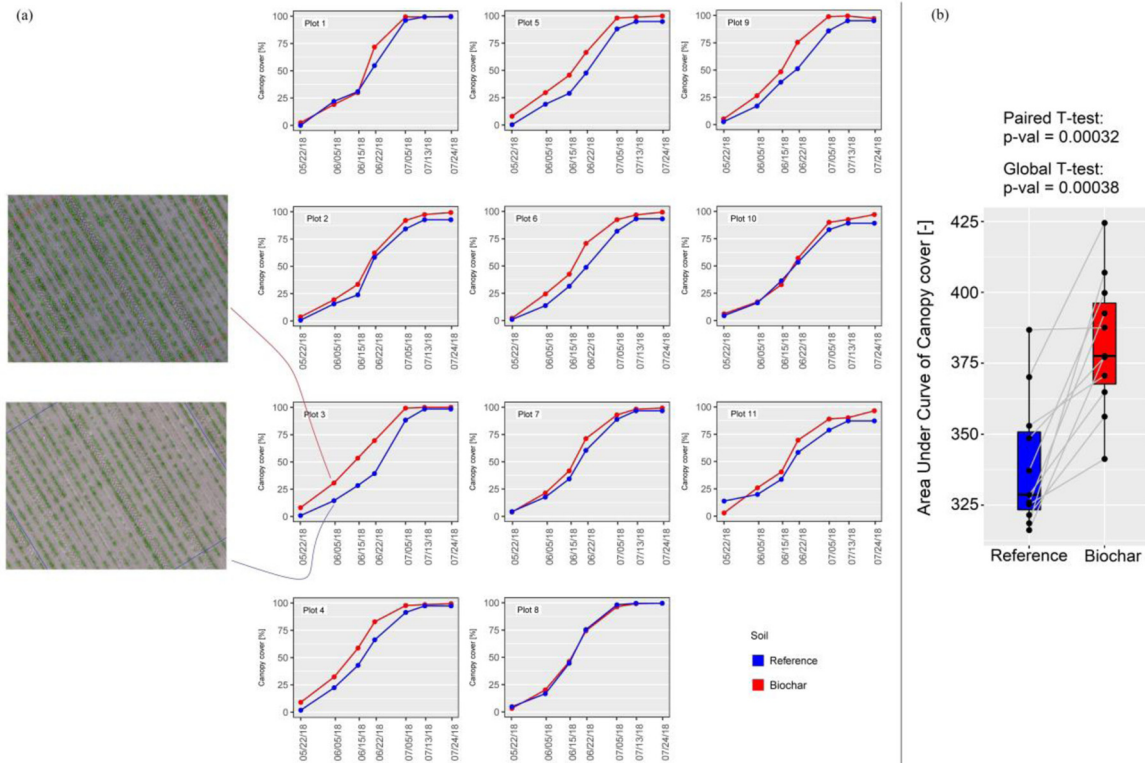
Fig. 5. (a) Temporal evolution of canopy cover for the 11 pairs of chicory plots (biochar versus reference) within the study area. Image detail comparing the canopy cover between the reference and biochar-enriched plot 3 on the 5th of June 2018. (b) Box plot representation of the area under the curve of the canopy cover graphs. The horizontal black line represents the median value, surrounded by box edges presenting the 25th and 75th percentiles. The black circles represent the experimental plots of each pair and the grey line between the points compares the corresponding reference and biochar-enriched plots of each pair. (For interpretation of the references to colour in this figure legend, the reader is referred to the web version of this article).

significant (Kendall's τ coefficient = 0.55, p-value$_{(Kendall)}$ = 0.044). Delta soil total nitrogen displayed a non-significant but still fairly clear relationship (R^2 = 0.40, p-value$_{(F\text{-}test)}$ = 0.066) with the delta AUC of canopy cover when the outliers were omitted (Fig. 6e). The obtained correlation was statistically significant (Kendall's τ coefficient of 0.4, p-value$_{(Kendall)}$ = 0.014). In contrast, no significant relationship was found between delta AUC of canopy cover and delta C/N atomic ratio (p-value$_{(F\text{-}test)}$ = 0.277) (Fig. 6f).

3.3.2. Multispectral vegetation indices

The impact of biochar presence on the narrow-band multispectral vegetation indices (as given in Table 2) for the four recording dates in July and August is presented in Table 3. In general, no significant difference of the vegetation indices was observed between the biochar-enriched and reference plots (p-value > 0.1). Concerning the WDVI imagery, the significant p-values obtained from the paired *t*-test towards the end of the growing season, confirmed that the influence of biochar presence can be captured by the UAV-based WDVI imagery. Comparisons of WDVI imagery between the reference and biochar-enriched plots for the four multispectral recording dates are shown in Fig. 7. Significant differences were observed between reference and biochar-enriched plots in the last two acquisitions at the end of July (p-value = 0.09647) and in August (p-value = 0.00931). It is worth noting that the observed WDVI differences were normally distributed allowing the use of a statistical paired *t*-test (plots not shown). Nevertheless, the rest of the selected narrow-band vegetation indices were highly affected by the crop saturation at the maturity stage and were not able to illustrate alterations associated to biochar presence.

Biochar showed a negative influence (lower median values of WDVI in Fig. 7) on crop status in terms of health and greenness over the maturity phase using multispectral imagery. Moreover, the rest of the

examined multispectral vegetation indices corroborated this negative effect of biochar on crop spectral information for each recording date (graphs not shown). The negative impact of biochar presence is more significant in August as leaves gradually lost their greenness and began yellowing (Table 3). This finding contrast with the positive impact of biochar presence on the evolution of crop canopy cover measured by RGB imagery (Section 3.3.1). However, in the present study a detailed evaluation of how biochar could have affect crop health in the senescence phase is still missing. And as such, future research focusing on how multispectral information, gathered during this critical phase of the season, could be used to support sustainable agricultural management is highly favourable.

Noting the aforementioned caveats, we were interested in testing whether the observed discrepancies in the UAV-based WDVI imagery (Fig. 7) could be explained by the different SOC and total nitrogen concentrations between the paired plots. Comparison of UAV-based WDVI and laboratory measurements of SOC and nitrogen contents for all the experimental plots exhibited no-significant correlations (Fig. 8a–c). After removing the two identified outliers (i.e. plots 1 and 3), the relationship between delta AUC of WDVI and delta SOC improved (R^2 = 0.21, p-value$_{(F\text{-}test)}$ = 0.100; Kendall's τ coefficient = 0.43, p-value$_{(Kendall)}$ = 0.111) as presented in Fig. 8d. Similarly, the relationship between delta AUC of WDVI and delta total nitrogen slightly improved when the outliers were omitted (R^2 = 0.18, p-value$_{(F\text{-}test)}$ = 0.251; Kendall's τ coefficient = 0.28, p-value$_{(Kendall)}$ = 0.291) as shown in Fig. 8e, though the improvement was not significant. In addition, there was still no significant relationship between delta AUC of WDVI and delta C/N atomic ratio without considering the outliers (Fig. 8f). Normalized difference red edge (NDRE) index allows the estimation of canopy nitrogen concentration (Siegmann et al., 2012). However, the result indicated no correlation
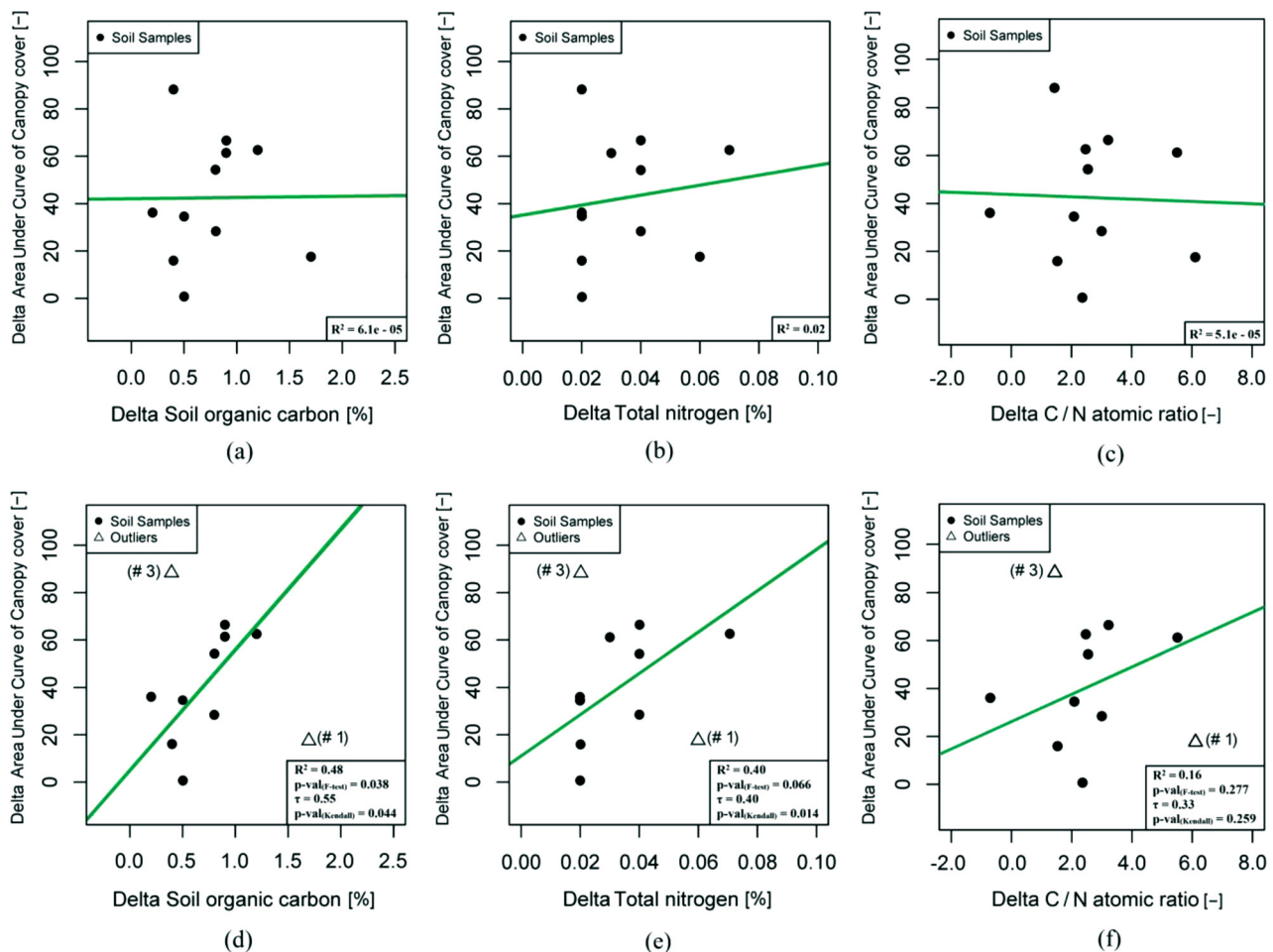
Fig. 6. Relationship between delta area under the curve of the unmanned aerial vehicle-based canopy cover time-series (y-axis) with delta soil organic carbon, delta total nitrogen, and delta C/N atomic ratio (x-axis) for all the 11 experimental pairs with (a-c) and without (d-f) considering the outliers. Delta is the computed difference between the reference and biochar-enriched plots of each pair. The black circles and triangles represent the soil samples and the detected outliers, respectively. The green line indicates the linear regression fit. In (d), (e), and (f) the outliers are excluded from the regression fits. (For interpretation of the references to colour in this figure legend, the reader is referred to the web version of this article).

Table 3
P-value results of the statistical paired t-test for the narrow-band vegetation indices derived from the unmanned aerial vehicle-based multispectral imagery.

Index Date	NDVI	WDVI	NDRE	CI_Red	CCCI
July 5	0.064	0.512	0.575	0.065	0.949
July 13	0.326	0.359	0.817	0.346	0.890
July 24	0.572	0.096	0.579	0.637	0.681
August 7	0.336	0.009	0.353	0.403	0.402

between delta AUC of NDRE and delta total nitrogen (plots not shown).

Interestingly, the relationships between delta area under the curve of UAV-based WDVI and measured SOC and total nitrogen contents were negative (Fig. 8). This result indicated that biochar presence decreases the plant health and greenness over the maturity phase, whereas there was a positive impact of biochar on crop growth during the green-up phase (Fig. 6).

3.3.3. Crop water stress and topographic wetness indices

The data recorded by the local meteorological station in the experimental field reported an extremely warm period (daily mean temperature of 18.5 °C) with rainfall close to zero from the beginning of July until mid-August that season (pers. comm. V. Burgeon). The western part of the experimental field is clearly less water stressed (Fig. 9a).

This is a consequence of the tall trees in the vicinity of the field, whose shadows were visible in the west of the experimental field (Fig. 1). The presence of shadows likely increased the crop evaporative cooling mechanism in the western part of the experimental field. A higher stressed zone is located in the middle of the field (Fig. 9a).

In addition, Fig. 9a highlights close similarities between the maps of the topographic wetness index on the 9th of May 2018 and mean crop water stress index. The south-western corner of the field, which had the highest rate for topographic wetness index, remained low in crop water stress index throughout the entire season. The associated map of mean crop water stress index (computed from the three thermal acquisitions) yielded a negative linear relationship with TWI map (R^2 = 0.40, p-value$_{(F-test)}$ = 0.001) considering all the experimental plots (Fig. 9a). The obtained correlation was statistically significant (Kendall's τ coefficient = 0.40, p-value$_{(Kendall)}$ = 0.008).

There was no notable effect of century-old biochar on topographic wetness index (p-value = 0.302) (Fig. 9b). The paired t-test of corrected mean crop water stress index indicated that biochar presence increased the mean crop water stress index from 4.6 °C in the reference plots to 5.0 °C for the biochar-enriched plots (Fig. 9b), although the observed difference was not statistically significant (p-value = 0.779). This increase of 0.4 °C could be attributed to the fact that the soil surface of the biochar-enriched plots is darker compared to the reference plots. This finding is in accordance with previous studies by Jeffery et al. (2015) and Gray et al. (2014) who documented that biochar addition did not
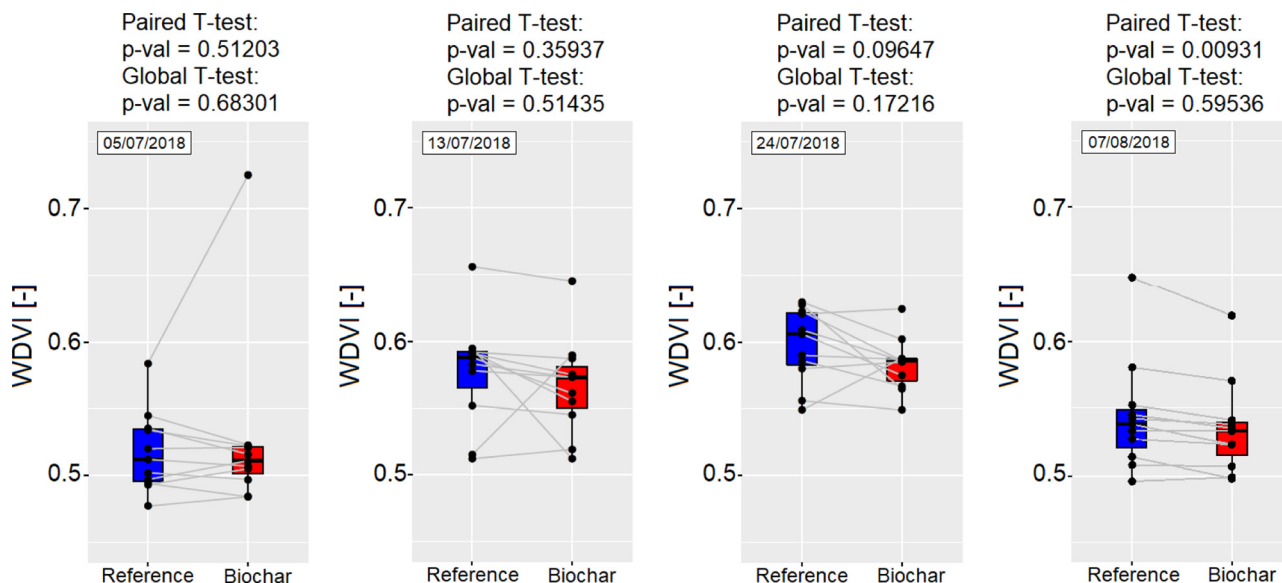
Fig. 7. The effectiveness of the weighted difference vegetation index in describing the impact of biochar presence on the radiometric information provided by the unmanned aerial vehicle-based multispectral imagery at the maturity phase. The horizontal black line represents the median value, surrounded by box edges presenting the 25th and 75th percentiles. The black circles represent the experimental plots of each pair and the grey line between the points compares the corresponding reference and biochar-enriched plots of each pair.
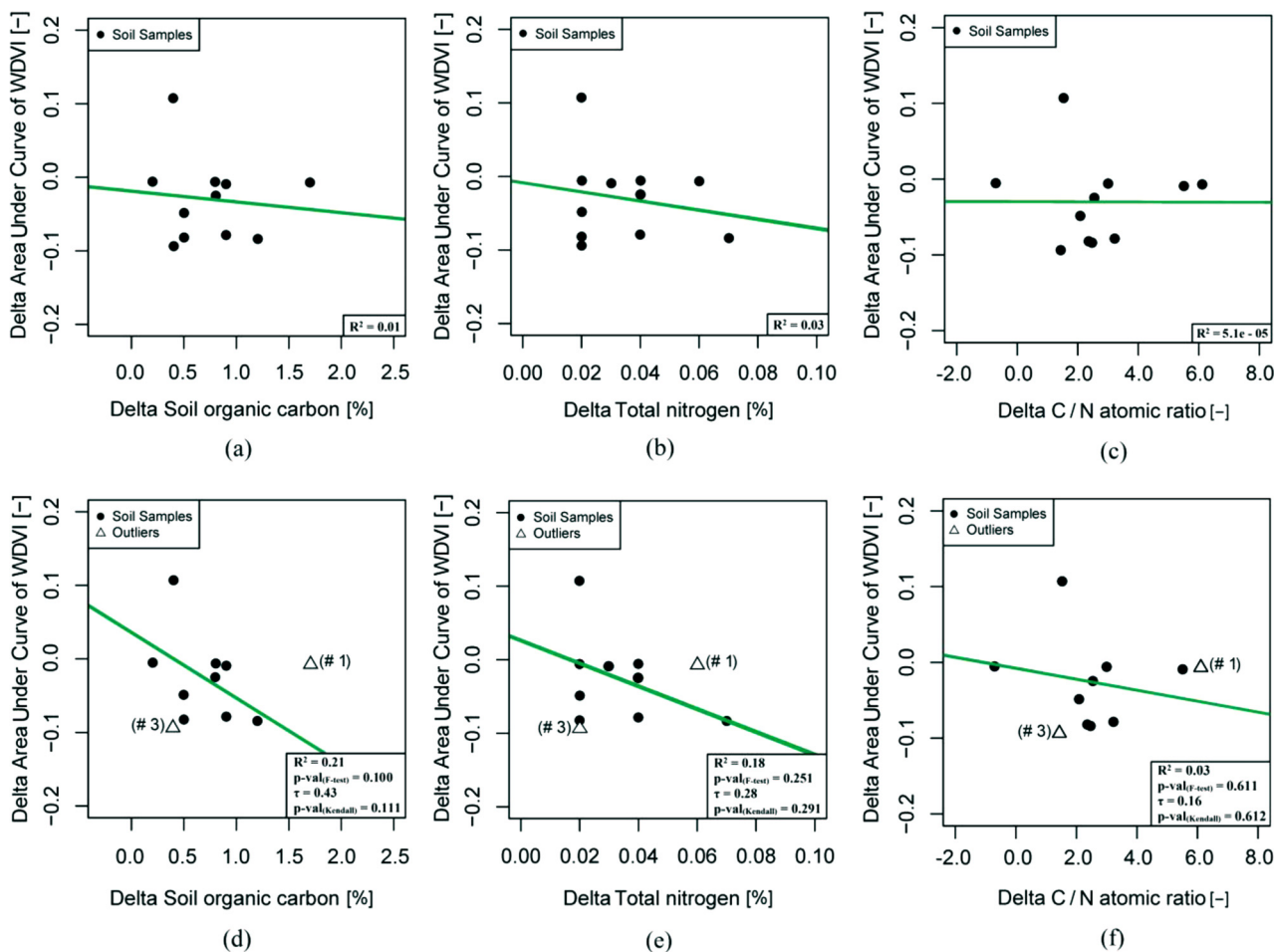

Fig. 8. Relationship between delta area under the curve of the unmanned aerial vehicle-based weighted difference vegetation index time-series (y-axis) with delta soil organic carbon, delta total nitrogen, and delta C/N atomic ratio (x-axis) for all the 11 experimental pairs with (a-c) and without (d-f) consideration of the outliers. Delta is the computed difference between the reference and biochar-enriched plots of each pair. The black circles and triangles represent the soil samples and the detected outliers, respectively. The green line indicates the linear regression fit. (For interpretation of the references to colour in this figure legend, the reader is referred to the web version of this article).
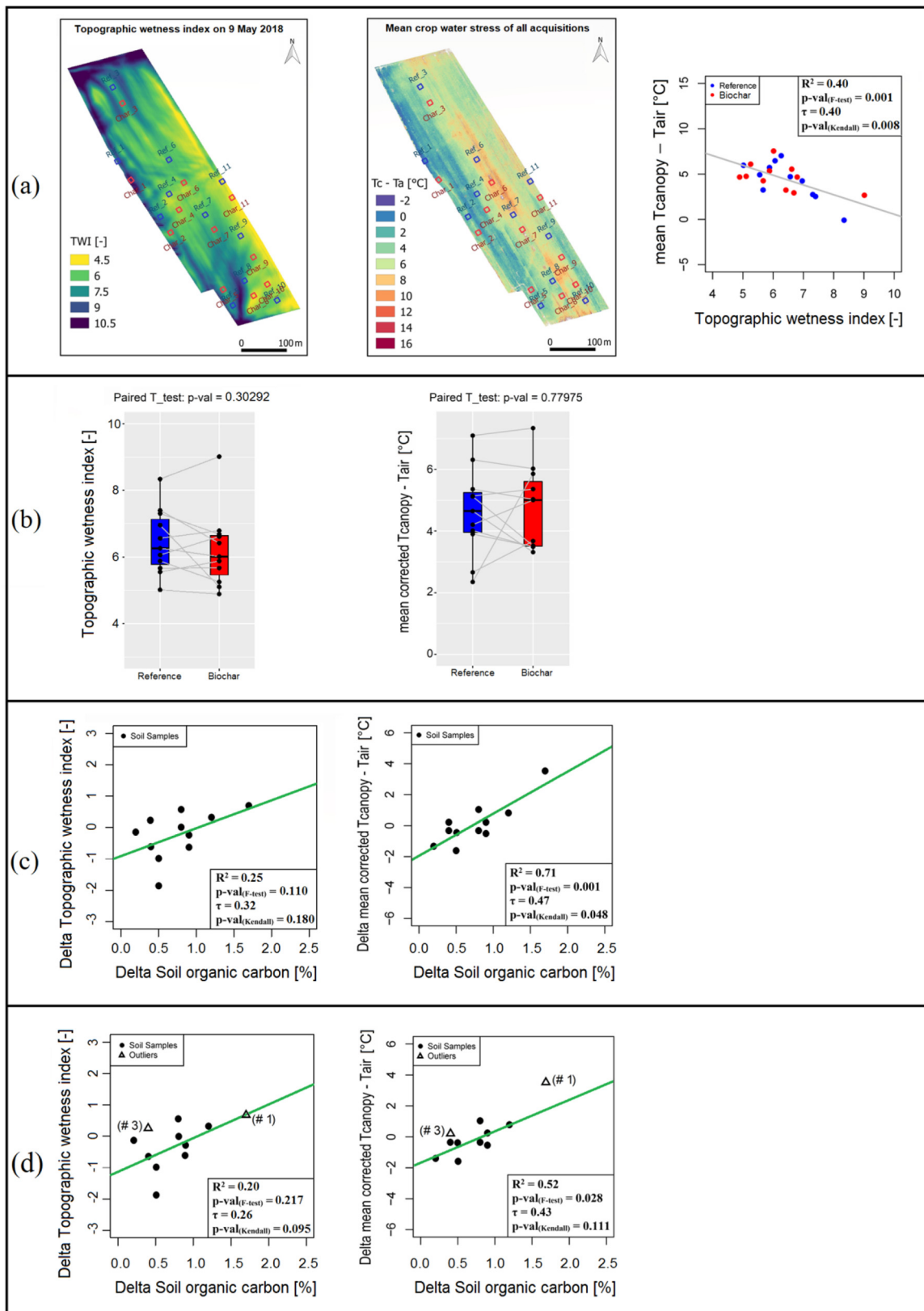
(caption on next page)

affect the plant available water content. However, our result cannot entirely rule out the previous evidence of higher soil and plant available water content as a consequence of biochar presence (Glaser et al., 2002; Abel et al., 2013; de la Rosa et al., 2014; Kerré et al., 2017) due to the limited number of thermal acquisitions throughout the season in the present study.

There was no significant relationship between delta SOC and delta topographic wetness index with or without considering the outliers (p-

Fig. 9. (a) Map of mean crop water stress index (mean Tcanopy – Tair) computed from the three thermal acquisitions along with the topographic wetness index (TWI) map on the 9th of May 2018 over the study field. Relationship between mean crop water stress index (y-axis) and TWI (x-axis), the blue and red circles represent the reference and biochar-enriched plots, respectively and the grey line indicates the linear regression fit. (b) Box plots represent topographic wetness index as wells as mean corrected crop water stress index after applying TWI amendment. The horizontal black line represents the median value, surrounded by box edges presenting the 25th and 75th percentiles, the black circles represent the experimental plots of each pair and the grey line between the points compares the corresponding reference and biochar-enriched plots of each pair. (c-d) Relationship between delta soil organic carbon (SOC) (x-axis) with delta topographic wetness index as well as delta mean corrected crop water stress index (y-axis) for all the 11 experimental pairs with (c) and without (d) inclusion of the outliers, delta is the computed difference between the reference and biochar-enriched plots of each pair, the black circles and triangles represent the soil samples and the detected outliers, respectively and the green line indicates the linear regression fit. (For interpretation of the references to colour in this figure legend, the reader is referred to the web version of this article).

value$_{(F-test)}$ of 0.110 and 0.217, respectively)(Fig. 9c–d). We repeated a similar exercise with the corrected crop water stress index values based on TWI imagery to study the isolated impact of biochar on crop water stress (Fig. 9c–d). Delta SOC exhibited a strongly significant relationship with delta mean corrected crop water stress index (R^2 = 0.71, p-value$_{(F-test)}$ = 0.001). The achieved correlation was slightly significant (Kendall's τ coefficient = 0.47, p-value$_{(Kendall)}$ = 0.048). In this context, it is worth mentioning that the attained relationship was weaker when the two identified outliers (i.e. plots 1 and 3) were omitted (R^2 = 0.52, p-value$_{(F-test)}$ = 0.028; Kendall's τ coefficient = 0.43, p-value$_{(Kendall)}$ = 0.111) as shown in Fig. 9c–d. The identified positive relationship between delta SOC and delta crop water stress underlines the previous finding of Schneider et al. (2020) who concluded that biochar leads to lower available water contents under dry conditions. However, it is important to bear in mind that characterization of the soil pore size distribution is needed in order to draw conclusions as regards this kind of effects (Atkinson et al., 2010; Minasny and McBratney, 2018).

There was no significant relationship between mean crop water stress index and root yields for neither the reference plots nor the biochar-enriched plots (p-value$_{(F-test)}$ of 0.312 and 0.632, respectively) (Fig. 10a). However, the reference plots characterized by the higher water stress values (the six identified blue circles in Fig. 10c) showed a strong negative relationship with root yields (R^2 = 0.70, p-value$_{(F-test)}$ = 0.035). The obtained correlation was statistically significant (Kendall's τ coefficient of 0.86, p-value$_{(Kendall)}$ = 0.016). However, the higher stressed biochar-enriched plots exhibited no significant relationship with root yields (p-value$_{(F-test)}$ = 0.417) (Fig. 10c).

On the other hand, leaf yield was strongly associated with the mean crop water stress index of all the reference plots (Kendall's τ coefficient of 0.45, p-value$_{(Kendall)}$ = 0.060) as well as all the biochar-enriched plots (Kendall's τ coefficient of 0.56, p-value$_{(Kendall)}$ = 0.016) as shown in Fig. 10b. In contrast, no significant relationship was found between leaf yield and mean crop water stress index in the higher stressed plots, neither for the reference nor the biochar sites (p-value$_{(F-test)}$ of 0.507 and 0.648, respectively) (Fig. 10d).

Our results showed that the presence of biochar did not increase the harvested crop yield, neither roots or leaves yield, under the stressed conditions (Fig. 10). This finding is in contradiction with Kerré et al. (2017) who reported an increased yield of maize along with a reduced water stress across three charcoal-enriched plots under similar pedological and climatic conditions.

The main objective of this research was to assess the long-term effects of biochar on crop growth, using high-resolution UAV-based remote sensing data, which may support climate-smart agriculture practices in the context of adaptation and mitigation to climate change. Until now many studies have explored the potential of biochar in maintaining soil organic matter and soil water holding capacity, enhancing soil fertility, reducing crop water stress, and improving crop productivity through quantitative meta-analysis (e.g. Jeffery et al., 2015). This paper presented a proof of concept of using UAV-based imageries in evaluating the effects of century-old biochar on crop growth and crop water stress in combination with *in situ* and laboratory measurements.

4. Conclusion

We highlighted a significant impact of century-old biochar on a soil-plant system based on UAV imageries. The assessment performed here focused on the temporal dynamics of chicory crop growth curves using RGB imagery. We concluded a detectable positive impact of biochar on chicory canopy cover during the growing season. UAV-based multi-spectral imagery underlined the negative influence of biochar on crop greenness using narrow-band vegetation indices, especially WDVI over the maturity period. It was verified that high-resolution UAV-based remote sensing can aid our understanding of the crop dynamics throughout the growing season which might be difficult with traditional field work.

In summary, biochar seems to slightly reinforce leaf length over the growing season as measured by *in situ* data. Biochar effects on root biophysical traits such as root length or yield were not perceptible.

Despite the hypothesis that biochar could increase the soil water retention, as would be the case in most wet conditions, century-old biochar in our study significantly increased the crop water stress at the end of the growing season derived from the UAV-based thermal imageries. In addition, it was found that topographic elements such as the topographic wetness index could contribute to the imposed crop stress levels towards the growing season. Future studies should evaluate how well these results can be generalised explicitly considering the actual field conditions.

To our knowledge this is the first paper to investigate the impact of century-old biochar on crop growth by remote sensing technology. The proposed approach using high spatial and temporal resolution UAV imagery is only suitable for monitoring single small size fields in the order of a few hectares. Further investigation should repeat the same tests across a wider range of crops and under contrasting weather conditions. Use of manned aircrafts or satellite images (e.g. Sentinel-2 and TripleSat) could bridge this gap of knowledge thanks to their fine spatial and temporal characteristics.

Author statement

RHD and AD conceived and designed the experiments. RHD performed the field and laboratory measurements together with AD, VB, JF, and EPG. RHD processed and analysed the data with assistance from AD, JF, and JM. BT, JM, and JTC managed the project administration and funding acquisition. JTC led the coordination of CHAR project. RHD wrote the manuscript. RHD, AD, VB, JF, JTC, and JM contributed to the editing of the manuscript. RHD revised the manuscript with assistance from all other co-authors. All authors contributed to the conceptualization of this work.

Declaration of Competing Interest

None.
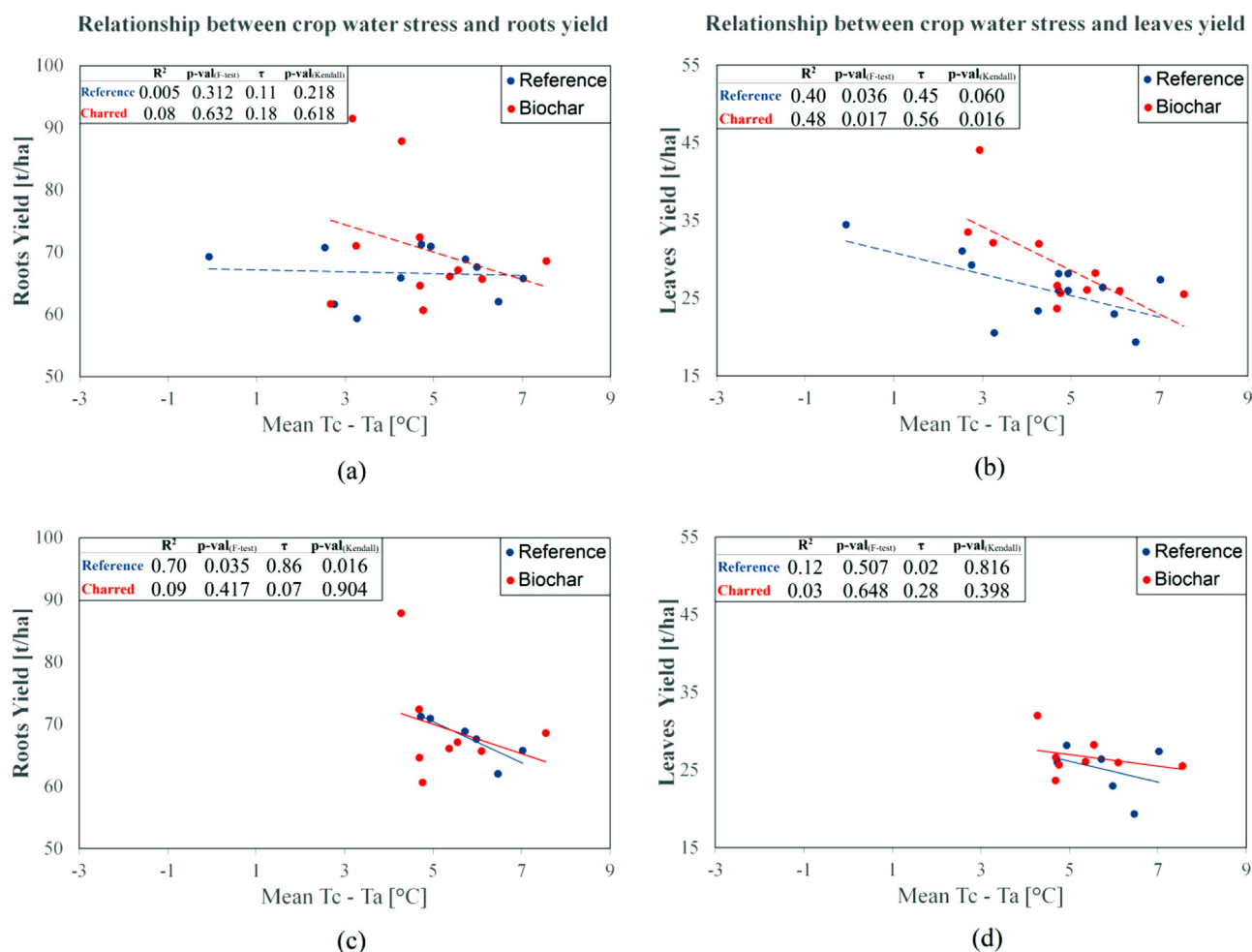
Fig. 10. Relationship between mean crop water stress index (mean Tc – Ta) computed from the three thermal acquisitions and in situ yield measurements of roots and leaves for all the 11 experimental pairs (a and b) as well as for only the higher stressed plots (c and d). The blue and red circles represent the reference and biochar plots respectively. The dashed and solid lines represent the linear regression fits considering all the experimental plots and only the higher stressed plots, respectively. (For interpretation of the references to colour in this figure legend, the reader is referred to the web version of this article).

References

Abawi, G., 1998. Project Reports 1998 J L Y L Integrated Pest Management. pp. 14456.

Abel, S., Peters, A., Trinks, S., Schonsky, H., Facklam, M., Wessolek, G., 2013. Impact of biochar and hydrochar addition on water retention and water repellency of sandy soil. Geoderma 202–203, 183–191. https://doi.org/10.1016/j.geoderma.2013.03.003.

Aksoy, H., Ozgur Kirca, V.S., Burgan, H.I., Kellecioglu, D., 2016. Hydrological and Hydraulic Models for Determination of Flood-Prone and Flood Inundation Areas 373. IAHS-AISH Proc. Reports, pp. 137–141. https://doi.org/10.5194/piahs-373-137-2016.

Bellvert, J., Zarco-Tejada, P.J., Girona, J., Fereres, E., 2014. Mapping crop water stress index in a 'Pinot-noir' vineyard: comparing ground measurements with thermal remote sensing imagery from an unmanned aerial vehicle. Precis. Agric. 15, 361–376. https://doi.org/10.1007/s11119-013-9334-5.

Berni, J.A.J., Zarco-Tejada, P.J., Sepulcre-Cantó, G., Fereres, E., Villalobos, F., 2009a. Mapping canopy conductance and CWSI in olive orchards using high resolution thermal remote sensing imagery. Remote Sens. Environ. 113, 2380–2388. https://

doi.org/10.1016/j.rse.2009.06.018.

Berni, J.A.J., Zarco-Tejada, P.J., Suárez, L., Fereres, E., 2009b. Thermal and narrowband multispectral remote sensing for vegetation monitoring from an unmanned aerial vehicle. IEEE Trans. Geosci. Remote Sens. 47, 722–738. https://doi.org/10.1109/TGRS.2008.2010457.

Biederman, L.A., Stanley Harpole, W., 2013. Biochar and its effects on plant productivity and nutrient cycling: a meta-analysis. Gcb Bioenergy 5, 202–214. https://doi.org/10.1111/gcbb.12037.

Clevers, J.G.P.W., 1989. The application of a weighted infrared-red vegetation index for estimating leaf area index by correcting for soil moisture. Remote Sens. Environ. 29, 25–37. https://doi.org/10.1016/0034-4257(89)90076-X.

Clevers, J.G.P.W., Kooistra, L., van den Brande, M.M.M., 2017. Using Sentinel-2 data for retrieving LAI and leaf and canopy chlorophyll content of a potato crop. Remote Sens. 9, 1–15. https://doi.org/10.3390/rs9050405.

Crane-Droesch, A., Abiven, S., Jeffery, S., Torn, M.S., 2013. Heterogeneous global crop yield response to biochar: a meta-regression analysis. Environ. Res. Lett. 8. https://doi.org/10.1088/1748-9326/8/4/044049.

de la Rosa, J.M., Paneque, M., Miller, A.Z., Knicker, H., 2014. Relating physical and chemical properties of four different biochars and their application rate to biomass production of Lolium perenne on a Calcic Cambisol during a pot experiment of 79 days. Sci. Total Environ. 499, 175–184. https://doi.org/10.1016/j.scitotenv.2014.08.025.

Fitzgerald, G.J., Rodriguez, D., Christensen, L.K., Belford, R., Sadras, V.O., Clarke, T.R., 2006. Spectral and thermal sensing for nitrogen and water status in rainfed and irrigated wheat environments. Precis. Agric. 7, 233–248. https://doi.org/10.1007/s11119-006-9011-z.

Gago, J., Douthe, C., Coopman, R.E., Gallego, P.P., Ribas-Carbo, M., Flexas, J., Escalona, J., Medrano, H., 2015. UAVs challenge to assess water stress for sustainable agriculture. Agric. Water Manag. 153, 9–19. https://doi.org/10.1016/j.agwat.2015.01.020.

García-tejero, I.F., Costa, J.M., Egipto, R., Durán-zuazo, V.H., Lima, R.S.N., Lopes, C.M., Chaves, M.M., 2016. Thermal data to monitor crop-water status in irrigated Mediterranean viticulture. Agric. Water Manag. 176, 80–90. https://doi.org/10.

1016/j.agwat.2016.05.008.

Gevaert, C.M., 2015. Generation of STRS by combining hyperspectral UAV and multi-spectral satellite and hyperspectral UAV imagery for precision agriculture application. IEEE J. Sel. Top. Appl. Earth Obs. Remote Sens. 8, 3140–3146.

Glaser, B., Lehmann, J., Zech, W., 2002. Ameliorating physical and chemical properties of highly weathered soils in the tropics with charcoal - a review. Biol. Fertil. Soils 35, 219–230. https://doi.org/10.1007/s00374-002-0466-4.

Grabs, T., Seibert, J., Bishop, K., Laudon, H., 2009. Modeling spatial patterns of saturated areas: a comparison of the topographic wetness index and a dynamic distributed model. J. Hydrol. 373, 15–23. https://doi.org/10.1016/j.jhydrol.2009.03.031.

Gray, M., Johnson, M.G., Dragila, M.I., Kleber, M., 2014. Water uptake in biochars: the roles of porosity and hydrophobicity. Biomass Bioenergy 61, 196–205. https://doi.org/10.1016/j.biombioe.2013.12.010.

Güereña, D., Lehmann, J., Hanley, K., Enders, A., Hyland, C., Riha, S., 2013. Nitrogen dynamics following field application of biochar in a temperate North American maize-based production system. Plant Soil 365, 239–254. https://doi.org/10.1007/s11104-012-1383-4.

Hardy, B., Cornelis, J.T., Houben, D., Leifeld, J., Lambert, R., Dufey, J.E., 2017a. Evaluation of the long-term effect of biochar on properties of temperate agricultural soil at pre-industrial charcoal kiln sites in Wallonia. Belgium. Eur. J. Soil Sci. 68, 80–89. https://doi.org/10.1111/ejss.12395.

Hardy, B., Leifeld, J., Knicker, H., Dufey, J.E., Deforce, K., Cornélis, J.T., 2017b. Long term change in chemical properties of preindustrial charcoal particles aged in forest and agricultural temperate soil. Org. Geochem. 107, 33–45. https://doi.org/10.1016/j.orggeochem.2017.02.008.

Hardy, B., Sleutel, S., Dufey, J.E., Cornelis, J.-T., 2019. The long-term effect of biochar on soil microbial abundance, activity and community structure is overwritten by land management. Front. Environ. Sci. 7, 1–14. https://doi.org/10.3389/fenvs.2019.00110.

Hernandez-Soriano, M.C., Kerré, B., Goos, P., Hardy, B., Dufey, J., Smolders, E., 2016. Long-term effect of biochar on the stabilization of recent carbon: soils with historical inputs of charcoal. GCB Bioenergy 8, 371–381. https://doi.org/10.1111/gcbb.12250.

Huete, A., 1988. A soil-adjusted vegetation index (SAVI). Remote Sensing of Environment 25 (3), 295–309. https://doi.org/10.1016/0034-4257(88)90106-X. ISSN 0034-4257.

Ihuoma, S.O., Madramootoo, C.A., 2017. Recent advances in crop water stress detection. Comput. Electron. Agric. 141, 267–275. https://doi.org/10.1016/j.compag.2017.07.026.

ISO 10694, 1995. 1995. Soil Quality – Determination of Organic and Total Carbon after Dry Combustion (elementary Analysis).

ISO 13878, 1998. 1998. Soil Quality – Determination of Total Nitrogen Content by Dry Combustion ("elemental Analysis").

Jackson, R.D., Reginato, R.J., Idso, S.B., 1977. Wheat Canopy Temperature: A Practical Tool. pp. 13.

Jeffery, S., Verheijen, F.G.A., van der Velde, M., Bastos, A.C., 2011. A quantitative review of the effects of biochar application to soils on crop productivity using meta-analysis. Agric. Ecosyst. Environ. 144, 175–187. https://doi.org/10.1016/j.agee.2011.08.015.

Jeffery, S., Meinders, M.B.J., Stoof, C.R., Bezemer, T.M., van de Voorde, T.F.J., Mommer, L., van Groenigen, J.W., 2015. Biochar application does not improve the soil hydrological function of a sandy soil. Geoderma 251–252, 47–54. https://doi.org/10.1016/j.geoderma.2015.03.022.

Johnson, B., Tateishi, R., Kobayashi, T., 2012. Remote sensing of fractional green vegetation cover using spatially-interpolated endmembers. Remote Sens. 4, 2619–2634. https://doi.org/10.3390/rs4092619.

Kendall, A.M.G., 1938. A New Measure of Rank Correlation Published by. Oxford University Press on behalf of Biometrika Trust Stable. URL: https://www.jstor.org/stable/2332226 30, 81–93.

Kerré, B., Willaert, B., Cornelis, Y., Smolders, E., 2017. Long-term presence of charcoal increases maize yield in Belgium due to increased soil water availability. Eur. J. Agron. 91, 10–15. https://doi.org/10.1016/j.eja.2017.09.003.

Kim, T.K., 2015. T Test as a Parametric Statistic.

Kopecký, M., Čížková, Š., 2010. Using topographic wetness index in vegetation ecology: does the algorithm matter? Appl. Veg. Sci. 13, 450–459. https://doi.org/10.1111/j.1654-109X.2010.01083.x.

Lehmann, J., Joseph, S., 2015. Biochar for environmental management: an introduction. Biochar Environ. Manage.: Sci. Technol. https://doi.org/10.4324/9781849770552.

Lehmann, J., Da Silva, J.P., Steiner, C., Nehls, T., Zech, W., Glaser, B., 2003. Nutrient availability and leaching in an archaeological Anthrosol and a Ferralsol of the Central Amazon basin: fertilizer, manure and charcoal amendments. Plant Soil 249, 343–357. https://doi.org/10.1023/A:1022833116184.

Major, J., Rondon, M., Molina, D., Riha, S.J., Lehmann, J., 2010. Maize yield and nutrition during 4 years after biochar application to a Colombian savanna oxisol. Plant Soil 333, 117–128. https://doi.org/10.1007/s11104-010-0327-0.

Malghani, S., Gleixner, G., Trumbore, S.E., 2013. Chars produced by slow pyrolysis and hydrothermal carbonization vary in carbon sequestration potential and greenhouse gases emissions. Soil Biol. Biochem. 62, 137–146. https://doi.org/10.1016/j.soilbio.2013.03.013.

Mastrolonardo, G., Calderaro, C., Cocozza, C., Hardy, B., Dufey, J., Cornelis, J.T., 2019.

Long-term effect of charcoal accumulation in hearth soils on tree growth and nutrient cycling. Front. Environ. Sci. 7, 1–15. https://doi.org/10.3389/fenvs.2019.00051.

Mikan and Abrams, 1986. Mechanisms Inhibiting the Forest Development of Historic Charcoal Hearths in Southeastern Pennsylvania. https://doi.org/10.1139/x26-213.

Minasny, B., McBratney, A.B., 2018. Limited Effect of Organic Matter on Soil Available Water Capacity. pp. 39–47. https://doi.org/10.1111/ejss.12475.

Montanarella, L., Lugato, E., 2013. The application of biochar in the EU: challenges and opportunities. Agronomy 3, 462–473. https://doi.org/10.3390/agronomy3020462.

Mulla, D.J., 2013. Twenty five years of remote sensing in precision agriculture: key advances and remaining knowledge gaps. Biosyst. Eng. 114, 358–371. https://doi.org/10.1016/j.biosystemseng.2012.08.009.

Parece, T.E., Campbell, J.B., 2015. Adv. Watershed Sci. Assess. https://doi.org/10.1007/978-3-319-14212-8.

Rouse Jr, J.W., Hass, R.H., Schell, J.A., Deering, D.W., Harlan, J.C., 1974. Texas a&m University Remote Sensing Center.

Schmidt, H., Karnieli, A., 2001. Sensitivity of vegetation indices to substrate brightness in hyper-arid environment: the Makhtesh Ramon Crater (Israel) case study. Int. J. Remote Sens. 22, 3503–3520. https://doi.org/10.1080/01431160110063779.

Schneider, A., Hirsch, F., Bonhage, A., Raab, A., Raab, T., 2020. Geoderma the soil moisture regime of charcoal-enriched land use legacy sites. Geoderma 366, 114241. https://doi.org/10.1016/j.geoderma.2020.114241.

Schwendenmann, C.M.L., 2015. Litterfall, Carbon and Nitrogen Cycling in a Southern Hemisphere Conifer Forest Dominated by Kauri (Agathis australis) During Drought. pp. 247–262. https://doi.org/10.1007/s11258-014-0432-x.

Seibert, J., Sørensen, R., Zinko, U., 2006. On the calculation of the topographic wetness index: evaluation of different methods based on field observations. Hydrol. Earth Syst. Sci. 10, 101–112.

Shapiro, A.S.S., Wilk, M.B., 1965. An Analysis of Variance Test for Normality (Complete Samples) 52. Published by : Oxford University Press on behalf of Biometrika Trust Stable, pp. 591–611.

Siegmann, B., Jarmer, T., Lilienthal, H., Richter, N., Selige, T., Sensing, R., 2012. Comparison of Narrow Band Vegetation Indices and Empirical Models From Hyperspectral Remote Sensing Data for the Assessment of Wheat Nitrogen Concentration.

Simon, J., Diego, A., Marija, P., Ana Catarina, B., Jan Willem van, G., Bruce, A.H., Frank, V., 2017. Biochar boosts tropical but not temperate crop yields. Environ. Res. Lett. 12, 53001.

Sohi, S.P., Krull, E., Lopez-Capel, E., Bol, R., 2010. A review of biochar and its use and function in soil. Advances in Agronomy, 1st ed. Elsevier Inc. https://doi.org/10.1016/S0065-2113(10)05002-9.

Stewart, C.E., Zheng, J., Botte, J., Cotrufo, M.F., 2013. Co-generated fast pyrolysis biochar mitigates green-house gas emissions and increases carbon sequestration in temperate soils. GCB Bioenergy 5, 153–164. https://doi.org/10.1111/gcbb.12001.

Tanriverdi, C., Atilgan, A., Degirmenci, H., Akyuz, A., 2017. Comparison of crop water stress index (Cwsi) and water deficit index (Wdi) by using remote sensing (Rs). Infrastruct. Ecol. Rural Areas 879–894. https://doi.org/10.14597/infraeco.2017.3.1.068.

Trout, T.J., Johnson, L.F., Gartung, J., 2008. Remote sensing of canopy cover in horticultural crops. HortScience 43, 333–337.

Trupiano, D., Cocozza, C., Baronti, S., Amendola, C., Vaccari, F.P., Lustrato, G., Di Lonardo, S., Fantasma, F., Tognetti, R., Scippa, G.S., 2017. The effects of biochar and its combination with compost on lettuce (Lactuca sativa L.) growth, soil properties, and soil microbial activity and abundance. Int. J. Agron. 2017. https://doi.org/10.1155/2017/3158207.

van Zwieten, L., Kimber, S., Morris, S., Chan, K.Y., Downie, A., Rust, J., Joseph, S., Cowie, A., 2010. Effects of biochar from slow pyrolysis of papermill waste on agronomic performance and soil fertility. Plant Soil 327, 235–246. https://doi.org/10.1007/s11104-009-0050-x.

Xia, T., Kustas, W.P., Anderson, M.C., Alfieri, J.G., Gao, F., McKee, L., Prueger, J.H., Geli, H.M.E., Neale, C.M.U., Sanchez, L., Alsina, M.M., Wang, Z., 2016. Mapping evapotranspiration with high-resolution aircraft imagery over vineyards using one-and two-source modeling schemes. Hydrol. Earth Syst. Sci. 20, 1523–1545. https://doi.org/10.5194/hess-20-1523-2016.

Yamato, M., Okimori, Y., Wibowo, I.F., Anshori, S., Ogawa, M., 2006. Effects of the Application of Charred Bark of Acacia mangium on the Yield of Maize, Cowpea and Peanut, and Soil Chemical Properties in South Sumatra, Indonesia. pp. 489–495. https://doi.org/10.1111/j.1747-0765.2006.00065.x.

Zarco-Tejada, P.J., González-Dugo, V., Williams, L.E., Suárez, L., Berni, J.A.J., Goldhamer, D., Fereres, E., 2013. A PRI-based water stress index combining structural and chlorophyll effects: assessment using diurnal narrow-band airborne imagery and the CWSI thermal index. Remote Sens. Environ. 138, 38–50. https://doi.org/10.1016/j.rse.2013.07.024.

Zipper, S.C., Loheide, S.P., 2014. Using evapotranspiration to assess drought sensitivity on a subfield scale with HRMET, a high resolution surface energy balance model. Agric. For. Meteorol. 197, 91–102. https://doi.org/10.1016/j.agrformet.2014.06.009.